AGU PUBLICATIONS

JGR

Journal of Geophysical Research: Oceans

RESEARCH ARTICLE

10.1002/2015JC010881

Key Points:
- Drawbacks of the *Wang and Shen* [2010] fluid layer model are identified
- Viscoelastic continuum models are calibrated with recently reported in situ data

Correspondence to:
J. E. M. Mosig,
jmosig@maths.otago.ac.nz

Citation:
Mosig, J. E. M., F. Montiel, and V. A. Squire (2015), Comparison of viscoelastic-type models for ocean wave attenuation in ice-covered seas, *J. Geophys. Res. Oceans*, *120*, 6072–6090, doi:10.1002/2015JC010881.

Received 29 MAR 2015
Accepted 21 JUL 2015
Accepted article online 24 JUL 2015
Published online 12 SEP 2015

Comparison of viscoelastic-type models for ocean wave attenuation in ice-covered seas

Johannes E. M. Mosig[1], Fabien Montiel[1], and Vernon A. Squire[1]

[1]Department of Mathematics and Statistics, University of Otago, Dunedin, New Zealand

Abstract Continuum-based models that describe the propagation of ocean waves in ice-infested seas are considered, where the surface ocean layer (including ice floes, brash ice, etc.) is modeled by a homogeneous viscoelastic material which causes waves to attenuate as they travel through the medium. Three ice layer models are compared, namely a viscoelastic fluid layer model currently being trialed in the spectral wave model WAVEWATCH III® and two simpler viscoelastic thin beam models. All three models are two dimensional. A comparative analysis shows that one of the beam models provides similar predictions for wave attenuation and wavelength to the viscoelastic fluid model. The three models are calibrated using wave attenuation data recently collected in the Antarctic marginal ice zone as an example. Although agreement with the data is obtained with all three models, several important issues related to the viscoelastic fluid model are identified that raise questions about its suitability to characterize wave attenuation in ice-covered seas. Viscoelastic beam models appear to provide a more robust parameterization of the phenomenon being modeled, but still remain questionable as a valid characterization of wave-ice interactions generally.

1. Introduction

The polar regions have undergone major transformations over the last three decades, with satellite and in situ observations revealing a dramatic decline of Arctic summer sea ice extent and volume [*Meier et al*., 2013; *Kwok and Rothrock*, 2009], and a modest increase in winter Antarctic sea ice extent with significant spatial variability [*Simpkins et al*., 2013]. The magnitude and trends of such changes can only be partially captured by contemporary climate models [*Stroeve et al*., 2007; *Jeffries et al*., 2013; *Tietsche et al*., 2014], suggesting that important physical processes are being neglected. Recent evidence has shown that ocean waves play an important role in controlling the morphology of polar sea ice, caused by larger expanses of open water opening up in the Arctic Basin where stronger winds can then create more energetic waves over increasing fetches [*Young et al*., 2011; *Thomson and Rogers*, 2014]. In particular, large wave events have recently been observed in situ to travel hundreds of kilometers into the ice-covered Arctic and Southern Oceans, with sufficient energy to break up the sea ice [*Kohout et al*., 2014; *Collins et al*., 2015]. As a result, there is currently considerable interest in characterizing the mechanisms governing the interactions between ocean waves and sea ice, and to parameterizing their effects in contemporary climate models and operational wave models (see *Rogers and Orzech* [2013] for the implementation into WAVEWATCH III®).

Near the ice edge, the ice cover is inhomogeneous and highly dynamic. It is composed of a mixture of ice floes, brash, and open water, and is commonly referred to as the marginal ice zone (MIZ). Waves penetrating the MIZ are scattered by the heterogeneous ice terrain and dissipated. The scattering process is conservative as it redistributes the wave energy spatially, so waves penetrating ice fields are gradually reflected, causing an apparent exponential decay of wave energy with distance from the ice edge. Much attention has been given to the development of realistic wave scattering models and extracting an attenuation coefficient characterizing the decay of wave energy (see the review papers of *Squire et al*. [1995] and *Squire* [2007, 2011] for a comprehensive discussion). A number of nonconservative physical processes, such as wave breaking, floe collisions and overrafting, turbulence, overwash, and sea ice roughness and inelasticity, induce additional decay of wave energy. The complexity of modeling such (nonlinear) processes and the lack of experimental data have prevented a quantification of their effects on wave attenuation in the MIZ. Instead, a parameterization of all sources of dissipation is commonly used to model nonconservative wave attenuation, also assumed to be exponential.

The waves-in-ice model (WIM) advanced by *Williams et al*. [2013a, 2013b] incorporates the most complete parameterization of wave attenuation due to both scattering and dissipative processes. The WIM describes the advection of a wave spectrum exponentially attenuated as it propagates in the MIZ. Attenuation of the spectrum due to scattering is provided by the two-dimensional model of *Bennetts and Squire* [2012], which describes ensemble-averaged multiple wave scattering by random arrangements of ice floe edges, where the floes are modeled as thin elastic plates. Additional attenuation is introduced as a dissipation parameter in the thin plate equation, following the approach of *Robinson and Palmer* [1990]. The WIM also predicts the change in floe size distribution due to wave-induced floe breakup, which in turn influences the attenuation of waves. Another approach, similar to WIM, was considered by *Doble and Bidlot* [2013], who parameterized the Wave Model (WAM) to include wave attenuation in the MIZ by scattering (using the model of *Kohout and Meylan* [2008]), and ice roughness dissipation (based on *Kohout et al*. [2011]).

A simpler and potentially more convenient approach is to model the surface ocean layer (including ice floes, brash ice, etc.) as a continuous homogeneous medium, described by a small number of rheological parameters. Wave propagation through the medium is then characterized by a dispersion relation, which provides the wavelength and attenuation coefficient of the wave modes supported by the medium. Such models are empirical and the rheological parameters are not related to the properties of sea ice, nor can they be measured independently. The parameters can be estimated by measuring all the other quantities of the model, e.g., wavelength, period, and attenuation, and solving an inverse problem. Although the continuum models have recently received much attention in the sea ice community, there is no evidence that this type of parameterization is a valid approach for modeling wave propagation in the MIZ. In particular, such models have not been tested against the more rigorous process-based models described above and very little experimental validation has been conducted. In this paper, we perform a comparison of three such rheological models and devise a calibration procedure for each model using wave data recently collected in the Antarctic MIZ [*Kohout and Williams*, 2013; *Kohout et al*., 2015].

To our knowledge, the first rheological model of sea ice goes back to *Greenhill* [1886], who used a simplified thin elastic plate model to derive a dispersion relation for a purely elastic solid ice cover. The dispersion relation for a thin elastic plate floating on inviscid and incompressible water was formally derived and solved by *Evans and Davies* [1968] and subsequently by *Wadhams* [1973, 1986] and *Fox and Squire* [1994]; the latter paper considering how surface waves are reflected from the transition between open water and solid ice. In its original form, the thin plate model only provides the wavelength of ice-coupled waves which then propagate without experiencing attenuation. Dissipation was introduced in the thin plate equation by *Squire and Allan* [1980] (for infinite water depth) who defined the constitutive relation of the ice cover using a four-parameter spring-dashpot model, and later by *Squire and Fox* [1992] who included a viscous term proportional to the plate's vertical velocity based on the model of *Robinson and Palmer* [1990] (Both these papers are focused on shore fast sea ice, as opposed to an open ice field). *Liu and Mollo-Christensen* [1988] parameterized dissipative effects using eddy viscosity in the water under a purely elastic ice cover. The rheological continuum models mentioned so far were intended to represent a solid ice cover or solitary ice floes, as opposed to a mixed ice layer. In contrast, the viscous layer models of *Keller* [1998] and *De Carolis and Desiderio* [2002] characterize wave propagation in a heterogeneous ice terrain. Recently, *Wang and Shen* [2010] extended Keller's model by including elastic effects. Their viscoelastic ice layer model, hereinafter referred to as the WS model, is a two-dimensional fluid with a prescribed constitutive relation derived from a simple spring-dashpot formulation. The WS model synthesizes the thin plate and viscous layer models described earlier, as limiting cases of a more general formulation. The WS model has only been calibrated with data from laboratory experiments by *Zhao and Shen* [2015], which cannot capture the full complexity of wave-ice interactions in ice-infested seas generally. This notwithstanding, it has been implemented in WAVEWATCH III® to describe the effect of sea ice on ocean wave attenuation [*Tolman and The WAVEWATCH III® Development Group*, 2014].

In this article, we identify several important deficiencies of the WS model. A central problem is the complexity of its dispersion relation, which predicts multiple wave modes that are difficult to categorize and interpret physically. For this reason, two viscoelastic beam models are also considered, which are more easily analyzed and calibrated. The first model is similar to the thin viscoelastic beam model of *Squire and Allan* [1980], although finite water depth and a simpler (i.e., two-parameter) constitutive relation are considered. The dispersion relation that we use resembles that proposed by *Fox and Squire* [1994], which is only modified by taking a complex (as opposed to real) elastic modulus, and by restricting it to two dimensions (replacing a plate

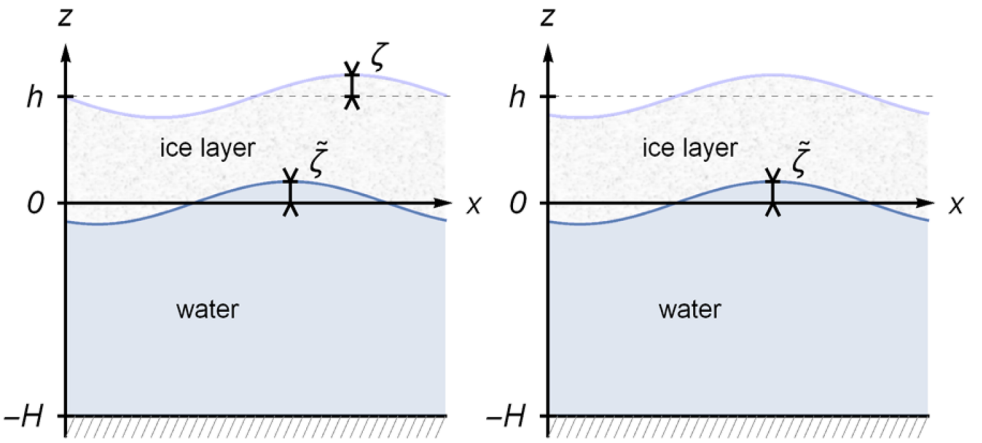

Figure 1. Sketch of (left) the WS viscoelastic fluid model and (right) the FS (or RP) viscoelastic thin beam model.

by a beam). Hereafter, we refer to this augmented model as the FS model. The second model is the two-dimensional version of the thin viscoelastic plate model considered by *Squire and Fox* [1992], which was derived earlier by *Robinson and Palmer* [1990] in a different context. Subsequently it is referred to as the RP model. The FS and RP models differ only in the way viscosity is introduced. In both models the water body beneath the water-ice mixture layer is described as an incompressible, inviscid fluid, replicating the WS model. We construct the FS model in order to satisfy the same deviatoric stress-strain relationship as the WS model, so the two models take the same rheological input parameters, allowing us to compare them directly.

The simplicity of rheological viscoelastic-type models is counterbalanced by the difficulty in estimating their parameters. Only sparse data sets exist that can be used to calibrate the models. Simultaneous measurements of wave period, attenuation rate, and wavelength are required to perform the calibration, which has never been achieved and may not be feasible with contemporary measurement techniques. In situ measurements typically use multiple wave buoys to extract attenuation rate and wave period [see e.g., *Wadhams et al*., 1988; *Meylan et al*., 2014], while attenuation rate and wavelength can be recovered using remote sensing observations, e.g., synthetic aperture radar (SAR) imagery [*Liu et al*., 1992]. The relationship between wave period and wavelength in ice-covered oceans (i.e., the dispersion relation) is not known, however. In the following, we estimate the rheological parameters of the WS, FS, and RP models using wave period and attenuation coefficients derived by *Meylan et al*. [2014] from the data collected by *Kohout and Williams* [2013]. A method is devised to estimate the wavelength which gives the best fit of the FS model to the experimental attenuation coefficients. Difficulties arise when using the WS model, due to the existence of multiple sets of rheological parameters satisfying the dispersion relation for each wave measurement, suggesting that the model may be inappropriate to parameterize wave attenuation due to ice in spectral wave models, such as WAVEWATCH III®.

The present article is structured as follows. After introducing basic preliminaries in section 2, we present the assumptions and boundary conditions that define the WS, FS, and RP models in section 3. The resulting dispersion relations of the three models are given in section 4, and general properties of their solutions are discussed in section 5. In section 6, we compare the WS and FS models directly for a range of parameters and analyze the regimes where the models agree and diverge. Thereafter, we present a method to calibrate the three viscoelastic models and one simpler viscous layer model using field data analyzed by *Meylan et al*. [2014] and discuss the corresponding fit to the data in section 7. Finally, we conclude our discussion in section 8 with a set of recommendations concerning the use of viscoelastic-type parameterizations in operational wave models.

2. Preliminaries

Consider a two-dimensional seawater domain of infinite horizontal extent, bounded above by a sea ice cover and bounded below by the seafloor. Cartesian coordinates (x, z) are defined with z pointing upward, as depicted in Figure 1. The equilibrium water-ice interface is located at $z = 0$ and the seafloor coincides

with $z=-H$. The surface ocean layer (including ice floes, brash ice, etc.) has uniform thickness h and is homogeneous with density $\rho=917\,\mathrm{kg\,m^{-3}}$. In the following, we refer to the surface ocean layer as the ice layer.

We consider the propagation of time-harmonic flexural gravity waves in the positive x direction, with amplitude proportional to $\exp(-\mathrm{i}\,\omega\,t)$, where ω is the angular frequency and t denotes time. The time-harmonic condition then allows us to replace $\partial_t=-\mathrm{i}\,\omega$ throughout. The seawater is assumed to be inviscid and incompressible with density $\tilde{\rho}=1025\,\mathrm{kg\,m^{-3}}$. Therefore, its motion is fully described by a complex velocity potential $\tilde{\phi}$ satisfying the Laplace equation

$$\nabla^2\tilde{\phi}=0, \tag{1}$$

and the linearized Bernoulli equation

$$\mathrm{i}\,\omega\,\tilde{\rho}\,\tilde{\phi}=\tilde{\rho}\,g\,z-\tilde{P}, \tag{2}$$

where $\tilde{P}$ is the water pressure and $g=9.8\,\mathrm{m\,s^{-2}}$ is the acceleration due to gravity.

At the rigid seafloor, the vertical velocity vanishes, i.e.,

$$\partial_z\tilde{\phi}=0 \quad (z=-H). \tag{3}$$

At the water-ice interface, the kinematic condition is given by

$$-\mathrm{i}\,\omega\,\tilde{\zeta}=\partial_z\tilde{\phi}=U_z \quad (z=0), \tag{4}$$

where U_z is the z component of the velocity vector field $\mathbf{U}$ of the ice layer and $\tilde{\zeta}$ is the elevation of the water-ice interface. The form of the dynamic condition depends on the ice model under consideration.

3. Viscoelastic Ice Layer Models

We consider three viscoelastic ice layer models as mentioned in section 1: (i) the viscoelastic fluid model of *Wang and Shen* [2010] (WS model), (ii) the thin viscoelastic beam model derived by introducing viscosity into the constitutive relation of the thin plate model of *Fox and Squire* [1994] and reducing it to two dimensions (FS model), and (iii) the beam version of the thin viscoelastic plate model of *Robinson and Palmer* [1990] (RP model).

To show the relation between the WS and FS models properly, it is necessary to split the stress tensor S and the strain tensor E of the ice layer into their deviatoric and volumetric parts, i.e., s and σ, and e and ε, respectively. These are related by

$$\mathsf{S}=\mathsf{s}+\sigma\mathsf{1}, \quad \sigma=\frac{1}{2}\,\mathrm{tr}\{\mathsf{S}\}, \quad \mathsf{s}=\mathsf{S}-\sigma\,\mathsf{1}, \tag{5}$$

$$\mathsf{E}=\mathsf{e}+\varepsilon\mathsf{1}, \quad \varepsilon=\frac{1}{2}\,\mathrm{tr}\{\mathsf{E}\}, \quad \mathsf{e}=\mathsf{E}-\varepsilon\,\mathsf{1}, \tag{6}$$

where 1 is the identity tensor and tr denotes the trace. The deviatoric part is the trace-free part of a tensor and describes volume-preserving deformations or forces. The volumetric part is proportional to the trace and describes shape-preserving deformations or forces. Note that *Wang and Shen* [2010] incorrectly refer to the deviatoric parts of the strain and strain rate tensors in their equation (4) as just strain and strain rate tensors.

3.1. WS Ice Layer Model

The WS model describes the ice as an incompressible, viscoelastic (and therefore non-Newtonian) fluid. The relationship between deviatoric stress and strain is modeled by the Kelvin-Voigt element, i.e., a spring and dashpot in parallel [see *Flügge*, 1975]. The deviatoric stress tensor is then given by

$$\mathsf{s}=2\,G\,\mathsf{e}+2\,\rho\,\eta\,\partial_t\,\mathsf{e}=2\,(G-\mathrm{i}\,\omega\,\rho\,\eta)\,\mathsf{e}=2\,G_\mathrm{V}\,\mathsf{e}, \tag{7}$$

where G is the elastic shear modulus of the ice layer and η is a viscosity parameter related to the dashpot constant. We have also introduced the complex Voigt shear modulus $G_\mathrm{V}=G-\mathrm{i}\,\omega\,\rho\,\eta$, which depends on frequency. The volumetric stress is simply given by $\sigma=-P$, where P is the pressure in the ice.

Following *Wang and Shen* [2010], we introduce a velocity potential ϕ and a stream function ψ to represent the x and z components of the particle velocity vector field **U**, which are

$$U_x = -\partial_x\phi - \partial_z\psi \text{ and } U_z = -\partial_z\phi + \partial_x\psi, \tag{8}$$

respectively. Using the equations of motion and the continuity equation, the potential ϕ and stream function ψ can be shown to satisfy:

$$-\mathrm{i}\,\omega\,\rho\,\phi = P - \rho\,g\,z, \tag{9}$$

$$\nabla^2\phi = 0, \tag{10}$$

and

$$-\mathrm{i}\,\omega\,\psi = \frac{\mathrm{i}\,G_\mathrm{V}}{\omega\,\rho}\,\nabla^2\psi. \tag{11}$$

Vanishing shear stress at the top and the bottom boundaries of the ice layer implies

$$0 = -2\,\partial_x\partial_z\phi + \partial_x^2\psi - \partial_z^2\psi \quad (z=0, h), \tag{12}$$

respectively. Using that $\partial_t\zeta = U_z$ at $z = h$, where ζ is the elevation of the ice-atmosphere interface (see Figure 1, left), the condition of vanishing normal stress at the ice-atmosphere interface can be written as

$$0 = \omega^2\,\phi + 2\,\frac{G_\mathrm{V}}{\rho}\left(-\partial_z^2\phi + \partial_x\partial_z\psi\right) + g(-\partial_z\phi + \partial_x\psi) \quad (z=h). \tag{13}$$

Finally, using (2), (9), the kinematic condition (4), and the dynamic condition $\mathrm{S}(\mathbf{z},\mathbf{z}) = \tilde{P}$ at $z = 0$, the potentials $\tilde{\phi}$, ϕ, and the stream function ψ can be related as follows:

$$\frac{\tilde{\rho}}{\rho}\,\tilde{\phi} = \left(1 - \frac{\tilde{\rho}}{\rho}\right) g\,\omega^2(-\partial_z\phi + \partial_x\psi) + \phi + 2\,\frac{G_\mathrm{V}}{\omega^2\,\rho}\left(-\partial_z^2\phi + \partial_x\partial_z\psi\right) \quad (z=0). \tag{14}$$

3.2. FS Ice Layer Model

The FS model describes the ice layer as an isotropic viscoelastic thin beam. We assume relation (6) relates deviatoric stress and strain as in the WS model. Volumetric stress and strain are related by Hooke's law $\sigma = 2\,K\,\varepsilon$, where K is the bulk modulus (the factor 2 is the dimension of space).

Neglecting rotational inertia, the viscoelastic version of the Euler-Bernoulli beam equation is given by

$$\frac{G_\mathrm{V}\,h^3}{6}\,(1+\nu)\,\partial_x^4\tilde{\zeta} = P - \rho\,g\,h + \omega^2\,\rho\,h\,\tilde{\zeta}, \tag{15}$$

where $\tilde{\zeta}$ is the elevation of the water-ice interface, and P is the difference between the atmospheric pressure from above and the water pressure from below. Moreover, $\nu = 0.3$ is the Poisson ratio of sea ice. This value is chosen such that the limiting case $\eta \to 0\,\mathrm{m}^2\,\mathrm{s}^{-1}$ to a purely elastic thin beam, is consistent with experimental measurements for solid ice. For different ice morphologies, another Poisson ratio could be chosen but, as this is effectively a rescaling of G_V, it is unnecessary.

Equation (15) is almost identical to the standard (purely elastic) Euler-Bernoulli beam equation, as we have simply replaced the shear modulus G by the complex Voigt shear modulus G_V. The validity of this substitution is a consequence of the correspondence principle of viscoelasticity [see *Flügge*, 1975].

Using the dynamic boundary condition of the FS model

$$\tilde{P} = -P \quad (z=0), \tag{16}$$

as well as equation (2), the kinematic condition (4), and the beam equation (15), the coupled water-ice boundary condition is given by

$$0 = \left[\frac{G_\mathrm{V}\,h^3}{6}\,(1+\nu)\,\partial_x^4 - \omega^2\,\rho\,h + \tilde{\rho}\,g\right]\partial_z\tilde{\phi} - \omega^2\,\tilde{\rho}\,\tilde{\phi} \quad (z=0). \tag{17}$$

3.3. RP Ice Layer Model

The RP model is similar to the FS model, as the two models only differ in the way viscous effects are introduced. Specifically, the RP model includes a friction term proportional to the vertical velocity in the equation of motion, while stresses and strains are related by the standard Hooke's law, i.e., $s=2G\,e$ and $\sigma=2K\,\varepsilon$. The thin viscoelastic beam equation is given by

$$\frac{G h^3}{6}(1+\nu)\,\partial_x^4\tilde{\zeta}=P-\rho g h+\omega^2\rho h\tilde{\zeta}+\mathrm{i}\omega\gamma\tilde{\zeta}, \tag{18}$$

where γ is the viscosity parameter which is distinct from the viscosity parameter η used in the WS and FS models.

The dynamic boundary condition of the FS model (16) also holds for the RP model. Therefore, the coupled ice-water equation is obtained in the same way as with the FS model, resulting in

$$0=\left[\frac{G h^3}{6}(1+\nu)\,\partial_x^4-\omega^2\rho h+\tilde{\rho} g-\mathrm{i}\omega\gamma\right]\partial_z\tilde{\phi}-\omega^2\tilde{\rho}\tilde{\phi}\quad(z=0). \tag{19}$$

4. Dispersion Relations

For each model, a dispersion relation can be derived from the governing equations and boundary conditions. Invoking separation of variables, plane wave ansatzes of the form $\exp(\mathrm{i}kx)\cosh(\beta z)$ and $\exp(\mathrm{i}kx)\sinh(\beta z)$ are used for the potential functions $\tilde{\phi}$, ϕ, and the stream function ψ, where k is the wave number and β depends on k (see *Wang and Shen* [2010] for details). After some algebra, the dispersion relation can be written in the form

$$D(Qgk\tanh(Hk)-\omega^2)=0, \tag{20}$$

for all three ice layer models considered. Note that in (20), D and Q are functions of k and ω.

4.1. WS Model

For the WS model, $Q=Q_{\mathrm{WS}}$, with

$$\begin{aligned}Q_{\mathrm{WS}}=&\Big(\sinh(hk)\sinh(h\chi)\times(\rho^4\omega^4(N^4-g^2k^2)+16\chi^2G_{\mathrm{V}}^4k^6)\\&+8\chi G_{\mathrm{V}}^2k^3N^2\rho^2\omega^2(1-\cosh(hk)\cosh(h\chi))\Big)\Big/\Big(gk\rho\tilde{\rho}\omega^2\\&(\rho^2\omega^2\sinh(h\chi)(gk\sinh(hk)-N^2\cosh(hk))\\&+4\chi G_{\mathrm{V}}^2k^3\cosh(h\chi)\sinh(hk))\Big)+1,\end{aligned} \tag{21}$$

where

$$N=\omega-\frac{2k^2G_{\mathrm{V}}}{\rho\omega},\qquad \chi^2=k^2-\frac{\tilde{\rho}\omega^2}{G_{\mathrm{V}}}. \tag{22}$$

Furthermore, $D=D_{\mathrm{WS}}$, with

$$\begin{aligned}D_{\mathrm{WS}}=&\frac{h}{g}\Big((N^2\cosh(hk)-gk\sinh(hk))\sinh(h\chi)\\&-\frac{4\chi G_{\mathrm{V}}^2}{\rho^2\omega^2}k^3\cosh(h\chi)\sinh(hk)\Big).\end{aligned} \tag{23}$$

Note that the term D_{WS} does not appear in the original equation by *Wang and Shen* [2010, equation (44)], although it was taken into account in their computations. We further remark that the dispersion relation of the WS model describes waves propagating at or in between two interfaces (water-ice and ice-atmosphere). The corresponding wave modes can be flexural modes (upper and lower surfaces are in phase), extensional modes (surfaces are in antiphase), or a perturbation of these two types of modes arising from viscous effects (surfaces are out of phase). This makes it harder to interpret the physical relevance of the wave modes predicted by the WS model.

4.2. FS Model

For the FS model, we derived $Q=Q_{FS}$, with

$$\begin{aligned} Q_{FS} &= \frac{G_V h^3}{6\tilde{\rho} g}(1+\nu)k^4 - \frac{\rho h \omega^2}{\tilde{\rho} g} + 1 \\ &= \frac{G h^3}{6\tilde{\rho} g}(1+\nu)k^4 - \frac{\rho h \omega^2}{\tilde{\rho} g} + 1 - \mathrm{i}\,\omega\,\rho\,\eta\,\frac{h^3}{6\tilde{\rho} g}(1+\nu)k^4, \end{aligned} \tag{24}$$

and $D=D_{FS}=1$. In the second equality of equation (24), we expanded $G_V=G-\mathrm{i}\,\omega\,\rho\,\eta$ so that the similarity with the RP dispersion relation (see section 4.3) is clearly evident. We observe that the dispersion relation is much simpler than that of the WS model. In addition, all the wave modes predicted by the FS model are flexural modes (upper and lower interfaces are always in phase, as required by the thin beam assumption).

4.3. RP Model

The dispersion relation of the RP model is almost identical to that of the FS model, as only the viscous terms differ. Here $Q=Q_{RP}$, with

$$Q_{RP} = \frac{G h^3}{6\tilde{\rho} g}(1+\nu)k^4 - \frac{\rho h \omega^2}{\tilde{\rho} g} + 1 - \frac{\mathrm{i}\,\omega}{\tilde{\rho} g}\gamma, \tag{25}$$

and $D=D_{RP}=1$. Note that the only difference with the FS dispersion relation is the last term of (25) which is proportional to ω, compared to being proportional to ωk^4 in (24).

5. Solutions of the Dispersion Relations

The three dispersion relations derived in section 4 have infinitely many complex solutions. Each solution k to the dispersion relation corresponds to a plane wave mode and can be written as

$$k=\kappa+\mathrm{i}\,\alpha=2\pi/\lambda+\mathrm{i}\,\alpha, \tag{26}$$

where λ is the wavelength and α is the attenuation rate of wave amplitude. We are only interested in forward propagating and decaying wave modes so that we only consider solutions in the first quadrant of the complex k-plane (i.e., $\lambda > 0$ and $\alpha \geq 0$). The solutions of the WS, FS, and RP models depend on five parameters: the shear modulus G, the viscosity (η for WS and FS models, and γ for the RP model), the wave period $T=2\pi/\omega$, the ice cover thickness h, and the water depth H.

For zero viscosity ($\eta=\gamma=0$), the FS and RP dispersion relations reduce to the standard thin elastic beam dispersion relation, which has one real solution, one complex solution (with positive real and imaginary parts), and infinitely many purely imaginary solutions in the first quadrant of the complex k-plane [see e.g., *Evans and Davies*, 1968; *Fox and Squire*, 1994]. For nonzero viscosity, the solutions of the thin viscoelastic beam dispersion relations (FS or RP) are slightly perturbed in the complex plane, so they all have positive real and imaginary parts. We label the perturbed real and complex solutions of the FS model k_1^{FS} and k_2^{FS}, respectively. Likewise, we define k_1^{RP} and k_2^{RP} for the RP model. The perturbed imaginary solutions of the FS and RP models are not of interest here, since they describe quasi-evanescent waves with insignificant geophysical relevance. The solutions of the FS model can be seen in Figure 2 (right) for values of the parameters $(G, \eta, T, h, H)=(10\,\mathrm{Pa},\ 1\,\mathrm{m^2\,s^{-1}},\ 6\,\mathrm{s},\ 1\,\mathrm{m},\ 100\,\mathrm{m})$. The solutions of the RP model behave similarly.

The solutions of the WS model are not as simply organized in the complex plane as those of the FS and RP models. In particular, setting the viscosity to zero we find a large number of complex solutions (with positive real and imaginary parts) scattered over the first quadrant, in addition to a large (probably infinite) number of imaginary solutions and several real solutions. As with the FS model, all the solutions are perturbed in the first quadrant of the complex plane when a viscosity term is introduced. Note that, in contrast to the FS and RP models, standard root finding methods fail in some cases due to the existence of local maxima nearby certain solutions. Consequently, special numerical treatment is needed to overcome this issue.

We give unique labels to the various solutions of the WS model at $(G, \eta, T, h, H)=(10\,\mathrm{Pa},\ 1\,\mathrm{m^2\,s^{-1}},\ 6\,\mathrm{s},\ 1\,\mathrm{m},\ 100\,\mathrm{m})$. This set has been chosen so that the solutions are well separated and can be identified in the contour plot shown in Figure 2 (left). The two factors of the dispersion relation (20) can be treated

separately. We designate the solutions to $D_{WS}=0$ (see equation (23)) by k_A^{WS} and k_B^{WS} and the solutions to $(Q_{WS}\, g\, k \tanh(H\, k)-\omega^2)=0$ by k_1^{WS}, k_2^{WS}, k_3^{WS}, k_4^{WS}, ordered by increasing distance from the origin. More solutions exist beyond the domain depicted in Figure 2, and very close to the imaginary axis, but they are not shown as they are not geophysically relevant. In principle, these solutions may become relevant as the parameters are changed, but in the following we disregard this possibility and focus on the solutions highlighted in Figure 2.

Wang and Shen devised two criteria to identify the dominant solution k_{dom}^{WS} of the dispersion relation that has most geophysical relevance. Specifically, they defined a solution to be dominant if (i) the wavelength is closest to the open water value, and (ii) the attenuation rate is the least among all modes. We also use these criteria, although for some parameter configurations no solution satisfies both criteria, in which case we keep criterion (i) only. In all the cases we simulated, we found that k_{dom}^{WS} is always k_1^{WS}, k_2^{WS}, or k_A^{WS}. In section 7, we show that (for the WS model) these criteria are inadequate, justifying our choice to present a larger set of solutions. In the FS and RP models, the dominant solution is always k_1^{FS} and k_1^{RP}, respectively.

6. Comparison of the WS and FS Models

The WS and FS models have been constructed using the same viscoelastic constitutive relation, allowing us to compare the solutions of the two corresponding dispersion relations directly to each other when they are provided with the same parameters. Viscosity is introduced differently in the RP model so only qualitative comparisons can be performed with the other models. Therefore, we do not include the solutions of the RP dispersion relation in the present analysis.

For comparing the solutions of the two models, we define the difference in magnitude between two predictions p and q of the two models by $|\log_{10}(p)-\log_{10}(q)|=|\log_{10}(p/q)|$. In the following, p and q are either wavelengths or attenuation rates. This measure does not presume a reference solution, instead it accounts for the magnitude of the quantities compared.

Since the parameter space is five dimensional, we can only investigate a small part of it. Of primary interest are the rheological parameters G and η, and the thickness h, since these describe the ice. All the statements and conclusions made in the following analysis have been confirmed for various other parameter sets and can therefore be generalized.

6.1. Shear Modulus

In Figure 3, we compare the solutions (i.e., wavelength λ and attenuation rate α) of the WS and FS models for a wide range of shear moduli, i.e., $1\,\text{Pa} \le G \le 10^{15}\,\text{Pa}$ (*Wang and Shen* [2010] considered $G \le 10^9\,\text{Pa}$ only). The other parameters are fixed to $\eta=0.05\,\text{m}^2\,\text{s}^{-1}$, $T=8\,\text{s}$, $h=0.5\,\text{m}$, and $H=100\,\text{m}$. On the left figure, the wavelength is scaled by the corresponding open water wavelength for finite depth, λ_0 say, which is the real solution of the open water dispersion relation $\omega^2-(2\pi/\lambda_0)\, g \tanh((2\pi/\lambda_0)\, H)=0$.

We observe that the wavelength of the dominant modes of the WS (red line) and FS (thick, gray line) models, denoted by λ_{dom}^{WS} and λ_1^{FS}, respectively, are remarkably similar across the range of shear moduli considered (see left figure), as their difference in magnitude is always smaller than 0.07. We found that they agree best for $10^6\,\text{Pa} \lessapprox G \lessapprox 10^8\,\text{Pa}$ where the difference in magnitude is less than 0.01.

In contrast, the attenuation rates (see right figure) only agree for $G \gtrapprox 10^7\,\text{Pa}$. For lower values of G, we observe significant discrepancy between the two models, with the WS model predicting an attenuation rate more than 4 orders of magnitude larger than that of the FS model for $G \lessapprox 10^5\,\text{Pa}$. We conjecture that in this regime, elastic forces become small and shear forces in the WS fluid model dominate. We note that it is possible to adjust the viscosity parameter η in the FS model (keeping it fixed in the WS model) such that k_1^{FS} agrees with k_{dom}^{WS} in both wavelength and attenuation for small G (see Figure 5, right), in which case the agreement for large G is lost.

We further observe a discontinuity in wavelength at $G \sim 10^5\,\text{Pa}$ and a corresponding maximum in attenuation for the dominant solution of the WS model (red curve). This feature is associated with a change of dominant solution, as $k_{dom}^{WS}=k_1^{WS}$ for $G \lessapprox 10^5\,\text{Pa}$ and $k_{dom}^{WS}=k_2^{WS}$ for larger shear moduli, i.e., the dominant WS solution jumps to another wave mode. This behavior is specific to the WS model.

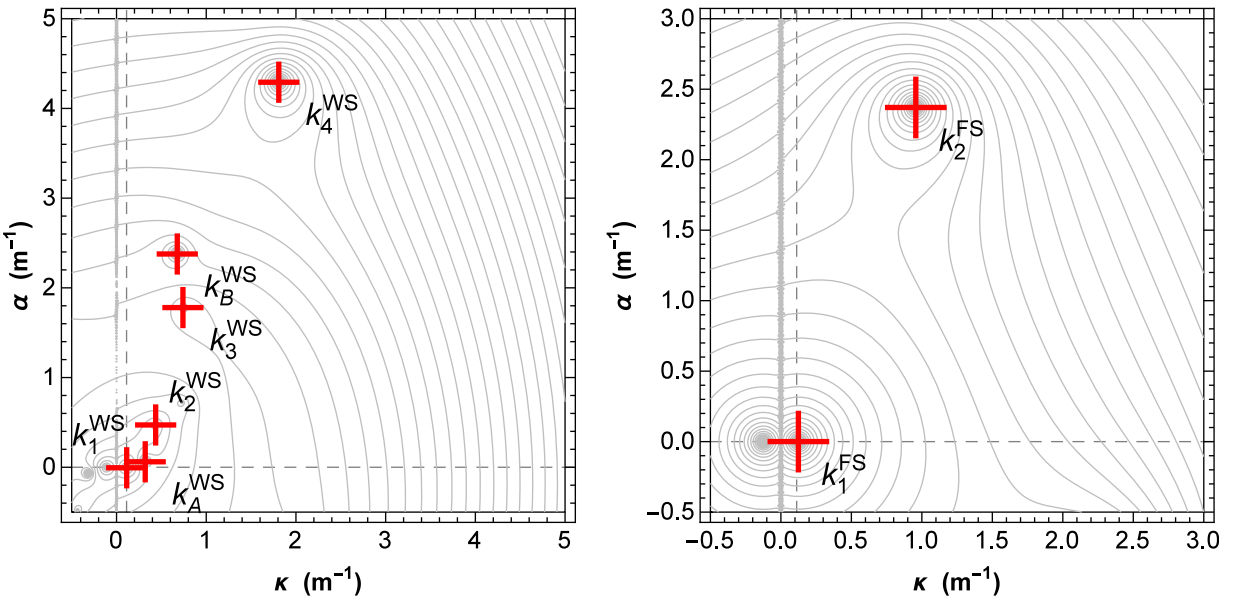

Figure 2. Selected contours of (left) $|D_{WS}(\kappa+i\alpha)|$ and (right) $|D_{FS}(\kappa+i\alpha)|$ with roots indicated by red crosses. Dashed lines indicate $\alpha=0$ and $\kappa=2\pi/\lambda_0$, where λ_0 is the open water wavelength. This contour plot was generated for the standard parameter set $(G, \eta, T, h, H)=(10\,\text{Pa},\ 1\,\text{m}^2\,\text{s}^{-1},\ 6\,\text{s},\ 1\,\text{m},\ 100\,\text{m})$.

We also depict k_3^{WS} and k_2^{FS} in Figure 3 (dot-dashed blue and thick dashed gray curve, respectively). We find that k_2^{FS} is qualitatively very similar to k_3^{WS} in the entire range of shear moduli, for both wavelength and attenuation rates. In terms of wavelength, the two solutions agree to within less than 0.45 orders of magnitude (0.15 for $G \gtrsim 10^4$ Pa). In terms of attenuation, they agree to within less than 0.3 orders of magnitude (0.1 for $G \gtrsim 10^3$ Pa).

6.2. Viscosity

We now fix G and vary the viscosity η in the range $10^{-3}\,\text{m}^2\,\text{s}^{-1} \le \eta \le 10^6\,\text{m}^2\,\text{s}^{-1}$. All other parameters remain as before. Note that *Wang and Shen* [2010] restricted their analysis to $\eta \le 1\,\text{m}^2\,\text{s}^{-1}$. In section 6.1, we showed that at $G=10^8$ Pa, k_2^{WS} is the dominant solution of the WS model and that k_1^{FS} is close to it in

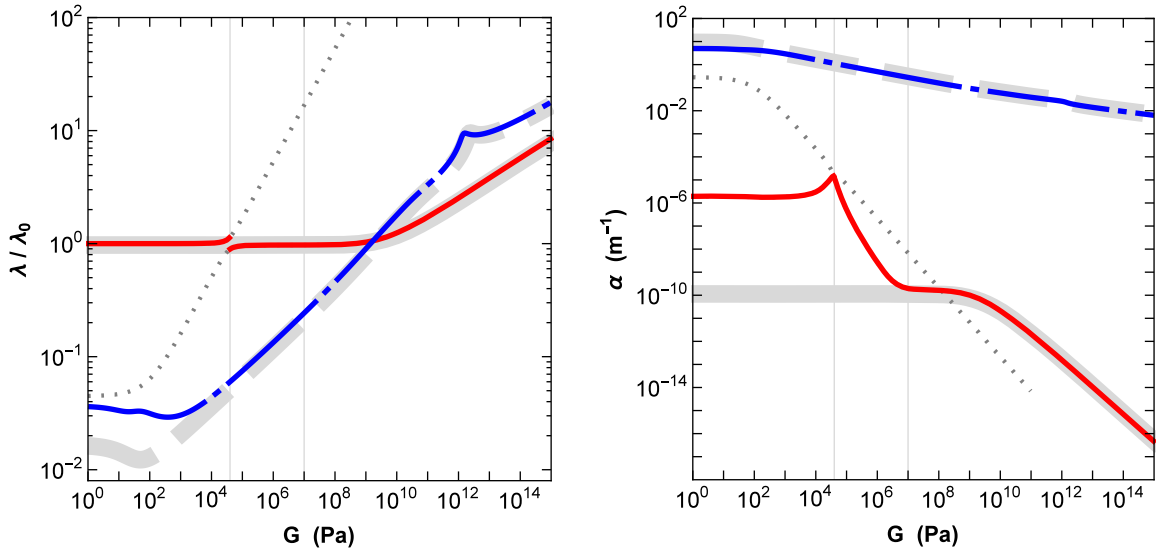

Figure 3. (left) Relative wavelengths λ/λ_0 and (right) attenuation coefficients α of various solutions of the FS and WS model for varying shear modulus G. Red (thin, solid) and blue (thin, dot-dashed) lines indicate the solutions k_{dom}^{WS} and k_3^{WS}, respectively. Thin gray dotted lines show how k_1^{WS} and k_2^{WS} continue when they are not dominant. Thick solid gray lines represent the dominant solution k_1^{FS} of the FS model. Thick dashed gray lines represent k_2^{FS}. For these plots, we chose $\eta=0.05\,\text{m}^2\,\text{s}^{-1}$, $T=8\,\text{s}$, $h=0.5\,\text{m}$, and $H=100\,\text{m}$.

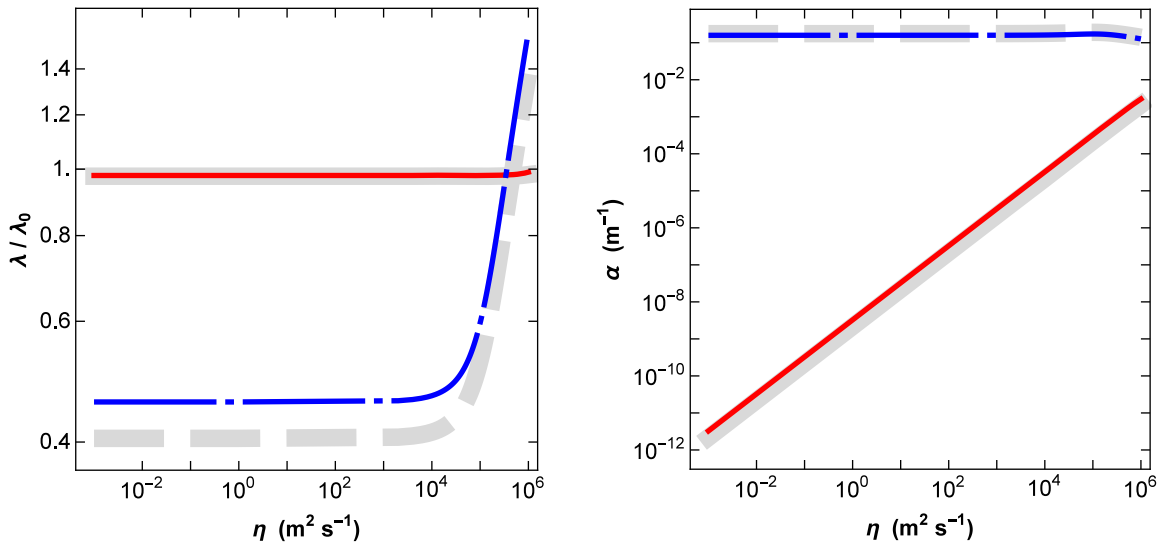

Figure 4. (left) Relative wavelengths λ/λ_0 and (right) attenuation coefficients α of various solutions of the FS and WS model for varying viscosity η at $G=10^8$ Pa. Line styles and other parameters are as in Figure 3.

both wavelength and attenuation rate. The solutions of the FS and WS models are depicted in Figure 4 for this value of the shear modulus.

The good agreement of the dominant solutions $k_{dom}^{WS}=k_2^{WS}$ and k_1^{FS} at $G=10^8$ Pa remains when the viscosity is changed over several orders of magnitude (red line and thick, solid, gray line, respectively). Specifically, the difference in magnitude stays below 0.005 and 0.18 for wavelengths and attenuation coefficients, respectively. The same holds for the solutions k_3^{WS} and k_2^{FS} (dot-dashed blue line and thick, dashed, gray line, respectively), as the difference in magnitude of the predicted wavelengths and attenuation coefficients remains below 0.062 and 0.045, respectively, over the entire range of viscosities.

We also calculated the dependence of the solutions on η for $G=10^2$ Pa, for which the models were found to differ in section 6.1. At this G, k_1^{WS} is the dominant solution of the WS model. Results are presented in Figure 5.

As we have shown in section 6.1, the dominant solutions k_{dom}^{WS} and k_1^{FS} agree in wavelength, but differ considerably in attenuation rate at $\eta=0.05\,\mathrm{m^2\,s^{-1}}$. This is true for $\eta \lesssim 10^2\,\mathrm{m^2\,s^{-1}}$, where the differences in magnitude are smaller than 0.013 for wavelength, but larger than 2.5 for attenuation rate. As η gets larger, however, the discrepancy in attenuation rates diminishes. For $\eta > 10^4\,\mathrm{m^2\,s^{-1}}$, the differences in magnitude stay below 0.003 and 0.3 for wavelength and attenuation rate, respectively. The secondary solutions k_3^{WS} and k_2^{FS} also agree better at large η. In terms of wavelength, the difference in magnitude lowers from 0.41 at $\eta=10^{-3}\,\mathrm{m^2\,s^{-1}}$ to 0.06 at $\eta=10^6\,\mathrm{m^2\,s^{-1}}$. The attenuation rates of k_3^{WS} and k_2^{FS} differ by less than 0.1 in magnitude for the entire range of η.

As discussed at the beginning of section 5, as $\eta \to 0\,\mathrm{m^2\,s^{-1}}$, the FS dispersion relation reduces to the thin elastic beam dispersion relation, with k_1^{FS} being the real solution and k_2^{FS} the complex solution with positive real and imaginary parts. Correspondingly, k_{dom}^{WS} becomes one of the real solutions of the WS model for zero viscosity, and k_3^{WS} stays off the real and imaginary axes.

6.3. Thickness

We now investigate the sensitivity of the solutions with respect to the ice cover thickness in the range $0\,\mathrm{m} \le h \le 10\,\mathrm{m}$. Results are shown in Figure 6 for $G=10^8$ Pa and in Figure 7 for $G=10^2$ Pa.

For both values of the shear modulus G considered, we observe that as $h \to 0$ m, the dominant wavelengths λ_1^{FS} and λ_{dom}^{WS} both approach the open water wavelength λ_0, and the dominant attenuation rates α_1^{FS} and α_{dom}^{WS} approach zero, as one would expect. The secondary solutions of both models also agree well, as both the real and imaginary parts of k_2^{FS} and k_3^{WS} are growing asymptotically to infinity in the limit. As h increases, the behavior of the solutions differ significantly for low and high shear modulus, however.

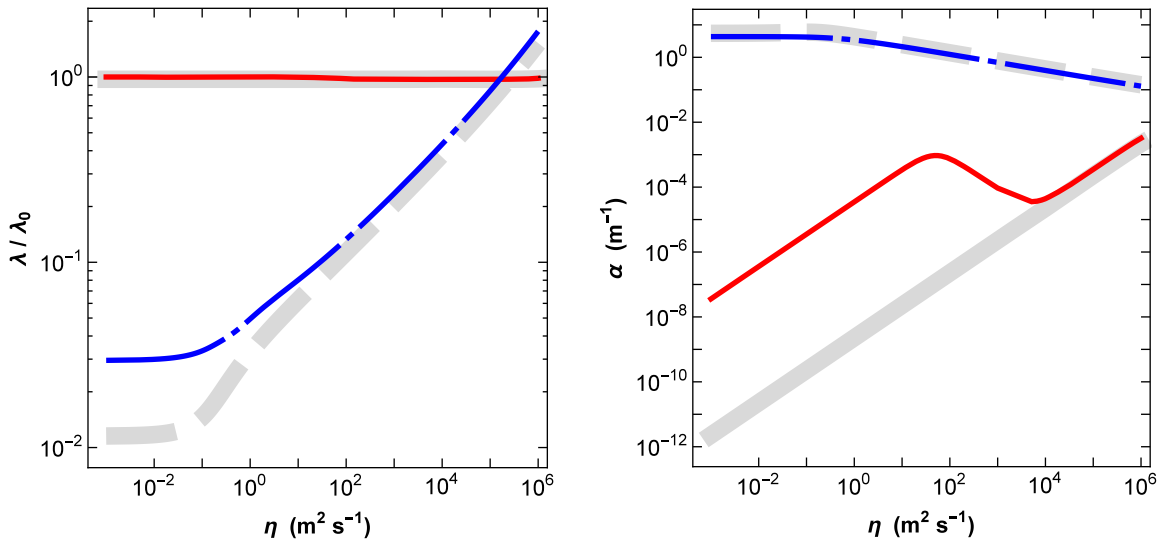

Figure 5. Same as Figure 4 but for $G=10^2$ Pa.

For $G=10^8$ Pa, we have a good agreement between the two models over the range of thicknesses considered in both wavelength and attenuation rate. The differences in magnitude remain below 0.035 and 0.2 for wavelength and attenuation rate, respectively.

For $G=10^2$ Pa, a significant discrepancy occurs in both wavelength and attenuation rate between the solutions of the WS and FS models. Specifically, the difference in magnitude of the dominant wavelength rises with increasing h from 3×10^{-4} at $h=0.01$ m to 0.36 at $h=10$ m. Meanwhile, the difference in magnitude of the dominant attenuation coefficients drops from 7.7 down to 0.3 over the same range of h. The differences in magnitude of the secondary solutions k_2^{FS} and k_3^{WS} show a complicated behavior for $h \lesssim 2$ m. However, as the thickness increases, the difference in magnitude of λ rises from 0.04 at $h=2$ m to 0.77 at $h=10$ m, while the difference in magnitude of α falls from 0.66 down to 0.11 over the same range of h. As in section 6.1, we conjecture that shear effects in the WS fluid model are significant compared to elastic effects in the regime of low G, which explains why the two models behave differently. We also note that the solutions of the WS model exhibit complicated features for $h \lesssim 2$ m, which is the regime of interest for the subsequent analysis. This behavior is difficult to explain physically. In contrast, the solutions of the FS model are well behaved in this range of thickness.

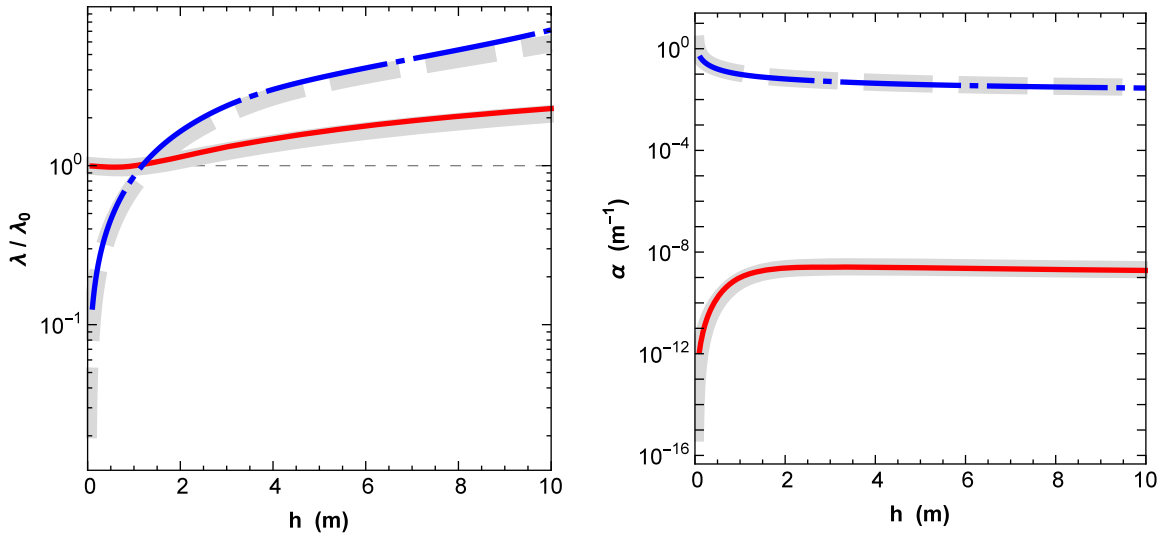

Figure 6. (left) Relative wavelengths λ/λ_0 and (right) attenuation coefficients α of various solutions of the FS and WS model for varying thickness h at $G=10^8$ Pa. Line styles and other parameters are as in Figure 3.

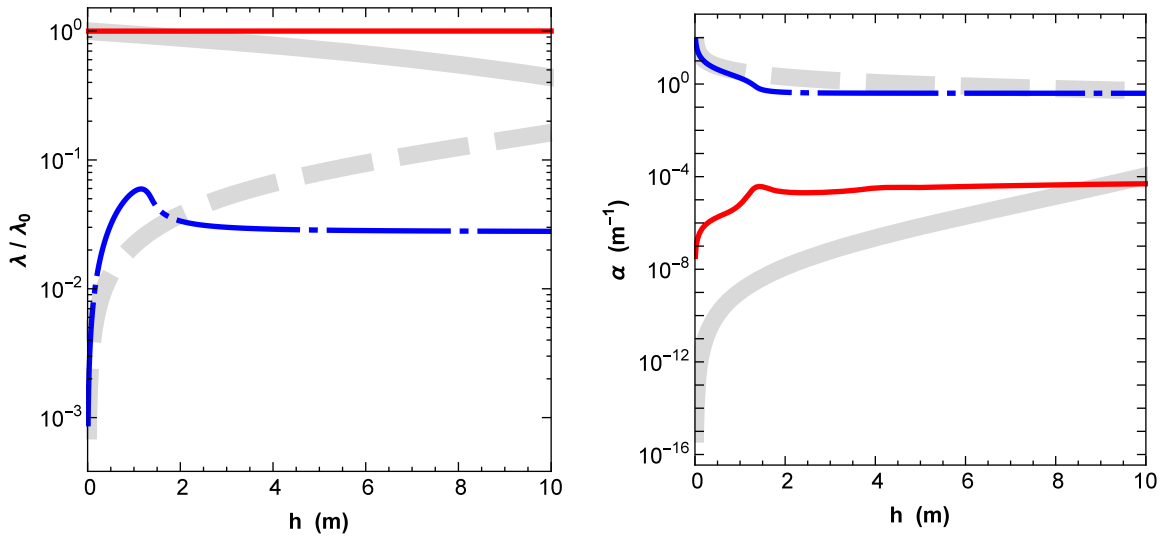

Figure 7. Same as Figure 6 but for $G=10^2$ Pa.

7. Model Calibration With Experimental Data

We now turn our attention to the problem of using the rheological models described in sections 3 and 4 to predict wave attenuation in ice-covered seas. The WS, FS, and RP models are empirical linear parameterizations of the combined dissipative and scattering mechanisms experienced by ocean waves due to the presence of sea ice. Consequently, the parameters of the models must be estimated so that the predicted wave attenuation rates are consistent with field observations. We devise a method to estimate the rheological parameters (G,η), for the WS and FS models, or (G,γ), for the RP model, using experimental data. The method is based on inverting the dispersion relation of each model for the rheological parameters, given the set (λ,α,T,h,H) of measured or estimated parameters.

To our knowledge, the wavelength λ, attenuation rate α, and period T of waves traveling through an ice field have never been measured simultaneously. Therefore, we rely on experimental measurements of wave energy attenuation coefficients against wave period. A synthesis of five experimental data sets collected in the Bering Sea and Greenland Sea between 1978 and 1983 was conducted by *Wadhams et al*. [1988]. However, we will use a more recent data set in which five contemporary wave sensors were deployed in the Antarctic marginal ice zone to measure wave energy attenuation and wave period [*Kohout and Williams*, 2013; *Kohout et al*., 2015]. The spectral analysis of the data was performed by *Meylan et al*. [2014] and we use the results presented in Figure 4 of that paper to calibrate the three rheological models considered here. The method used to estimate the corresponding wavelengths is described in the following subsections.

Throughout the following analysis, we assume a water depth of $H=4.3$ km, which is typical of the region where *Kohout et al*. [2014] conducted their experiments [*Wolfram Research, Inc*., 2014; *GEBCO*, 2014]. We also assume an ice thickness of 1 m. The sensitivity of the results with respect to ice thickness is discussed in section 7.1. Note that *Meylan et al*. [2014] provided decay rates for wave energy, while the attenuation rate α defined earlier is for wave amplitude. The difference has been taken into account by halving the decay rates of *Meylan et al*. [2014], since the wave energy is proportional to the square of the amplitude.

7.1. FS Model

A major advantage of the FS and RP models over the WS model is that their dispersion relations can be solved analytically for the rheological parameters and the solutions are unique. In the FS dispersion relation, $G_V=G-\mathrm{i}\,\omega\,\rho\,\eta$ appears only once, so a straightforward inversion yields

$$G_V=6\,\frac{\tilde{\rho}\,\omega^2\coth(H\,k)-g\,k\,\tilde{\rho}-h\,k\,\rho\,\omega^2}{h^3\,k^5\,(1+\nu)}. \tag{27}$$

Since the wavelength $\lambda=2\pi/\mathrm{Re}(k)$ has not been measured by *Kohout and Williams* [2013], we estimate it via an optimization procedure (described below in this section). Experiments by [*Wadhams and Holt*, 1991]

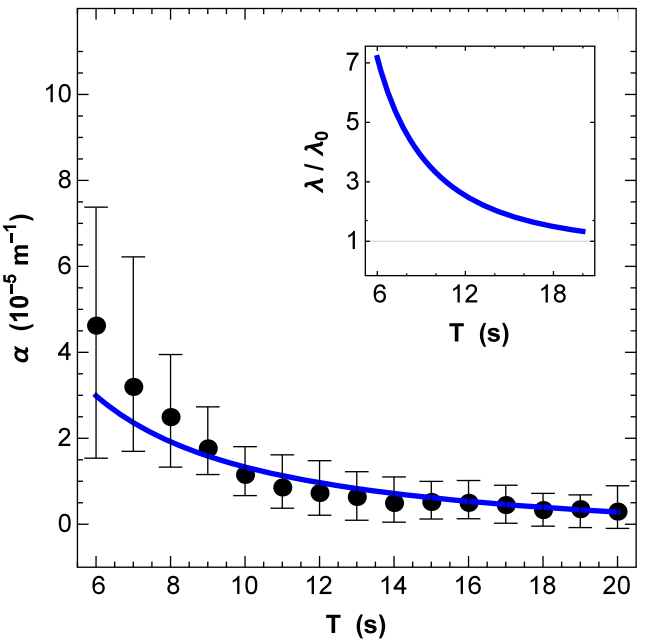

Figure 8. Comparison of attenuation rates versus wave period between predictions of the FS model (blue line) and experimental attenuation coefficients derived by *Meylan et al.* [2014]. The attenuation curve is generated for optimized wavelength $\lambda = 1.70\,\lambda_0$ and parameters $G = 4.9\times10^{12}$ Pa, $\eta = 5.0\times10^{7}$ m^2 s^{-1}, $h = 1$ m, and $H = 4300$ m. The inset displays the relative wavelength against wave period (i.e., the dispersion relation) for these estimated rheological parameters.

(section 6.3) using synthetic aperture radar (SAR) imaging have shown that the wavelength increases when a wave travels from open water into an ice field. Therefore, it is reasonable to assume that the wavelength at each period is greater than λ_0.

To simplify the analysis, we assume that $\lambda(T) = f\,\lambda_0(T)$, where f is a constant that we seek to optimize such that the FS model fits best to the data. We compute (27) for each measured period from 6 s to 20 s and for f from 1 to 2 with 0.05 increments. For each value of f, we then calculate the mean shear modulus $\bar{G}$ and mean viscosity $\bar{\eta}$ over all T. Note that weighting the mean with the inverse squared errors of the data gives almost identical results. We then compute $\alpha_1^{\mathrm{FS}}(T) = \mathrm{Im}(k_1^{\mathrm{FS}})(T)$ for each $(\bar{G}, \bar{\eta})$ pair and find that the FS model fits the data best when $f = 1.70$, in the least squares sense. The corresponding rheological parameters are $G = \bar{G} \approx 4.9\times10^{12}$ Pa and $\eta = \bar{\eta} \approx 5.0\times10^{7}$ m^2 s^{-1}.

The attenuation curve predicted by the FS model for the estimated parameters is plotted in Figure 8 alongside the experimental data. The model fits the data well within the error bars for all periods. We estimate the discrepancy between model and data by computing the weighted sum of squared deviations Δ. For the FS model, $\Delta \approx 0.4$.

The inset in Figure 8 shows the dispersion relation (i.e., wavelength versus wave period) for the rheological parameters computed above. We observe significant variations in relative wavelengths with $\lambda_1^{\mathrm{FS}} \approx 7.2\,\lambda_0$ at $T = 6$ s and $\approx 1.3\,\lambda_0$ at $T = 20$ s, which seems inconsistent with our initial assumption that $\lambda_1^{\mathrm{FS}} = 1.7\,\lambda_0$ for all wave periods. However, our calibration procedure allows for this apparent inconsistency: the assumption $\lambda_1^{\mathrm{FS}}(T) = 1.7\,\lambda_0(T)$ was satisfied when we solved (27) for each particular value of T considered, but this relationship does not hold once we fix $G = \bar{G}$ and $\eta = \bar{\eta}$ and use the dispersion relation to predict $\lambda_1^{\mathrm{FS}}(T)$. It is highly plausible that in reality the relative wavelength will be different for each period, and will depend on the type of ice cover. Only with a simultaneous measurement of T, λ, and α could a reliable test be designed.

Our choice of ice thickness for the model, i.e., $h = 1$ m, is somewhat arbitrary, although reasonable, as the measurements were made in first year ice with a thickness ranging from ~0.5 m to 1 m [see *Kohout et al.*, 2015]. It is therefore important to discuss the sensitivity of our calibration method with respect to this parameter. Doubling or halving the thickness, we were able to find new values of $\bar{G}$ and $\bar{\eta}$ that give a similar fit to the attenuation coefficients derived by *Meylan et al.* [2014], suggesting that thickness does not play a significant role in our analysis.

We observe that the shear modulus $G \sim 10^{12}$ Pa obtained using our calibration procedure is much larger than that of a solid ice cover (about 10^9 Pa). Moreover, the viscosity $\eta \sim 10^7$ m^2 s^{-1} is 9 orders of magnitude larger than 10^{-2} m^2 s^{-1}, a value determined experimentally by *Newyear and Martin* [1999] and *Wadhams et al.* [2004], noting that they fitted data to the viscous layer model of *Keller* [1998] which differs significantly from the FS model. Although our calibration may seem unphysical, we emphasize that the FS model is empirical and does not properly represent all processes causing wave attenuation, e.g., colliding and overrafting floes, turbulence, wave breaking, inelasticity, scattering, and other phenomena. In particular, the parameters cannot be measured directly as they do not represent observable physical processes.

Consequently, no restrictions on the acceptable values of the rheological parameters, except positiveness, can be imposed.

7.2. RP Model

As in the FS model, we are able to invert the dispersion relation of the RP model for the shear modulus G and viscosity γ analytically. After lengthy algebra, we obtain

$$\begin{aligned} G=&[6\,(\cos(2H\alpha)+\cosh(2H\kappa))\times((\alpha^2+\kappa^2)\,(g\tilde{\rho}-h\rho\omega^2)\cos(2H\alpha)\\ &-(\alpha^2+\kappa^2)\,(g\tilde{\rho}-h\rho\omega^2)\cosh(2H\kappa)+\tilde{\rho}\,\omega^2\,(\kappa\sinh(2H\kappa)-\alpha\sin(2H\alpha)))]\\ &/\,[h^3\,(\alpha^6-5\,\alpha^4\,\kappa^2-5\,\alpha^2\,\kappa^4+\kappa^6)\,(1+\nu)\times(\sin^2(2H\alpha)+\sinh^2(2H\kappa))], \end{aligned} \tag{28}$$

$$\begin{aligned} \gamma=&[(\cos(2H\alpha)+\cosh(2H\kappa))\times(4\,\alpha\,\kappa\,(\alpha^4-\kappa^4)\,(g\tilde{\rho}-h\rho\omega^2)\cosh(2H\kappa)\\ &-4\,\alpha\,\kappa\,(\alpha^4-\kappa^4)\,(g\tilde{\rho}-h\rho\omega^2)\cos(2H\alpha)+\tilde{\rho}\,\omega^2\,(\kappa\,(5\,\alpha^4-10\,\alpha^2\,\kappa^2+\kappa^4)\sin(2H\alpha)\\ &+\alpha\,(\alpha^4-10\,\alpha^2\,\kappa^2+5\,\kappa^4)\sinh(2H\kappa)))]/\,[(\alpha^6-5\,\alpha^4\,\kappa^2-5\,\alpha^2\,\kappa^4+\kappa^6)\,\omega\\ &\times(\sin^2(2H\alpha)+\sinh^2(2H\kappa))], \end{aligned} \tag{29}$$

where $\kappa=2\pi/\lambda$ and $\omega=2\pi/T$, as before.

We used the RP model to find an optimal wavelength in the same way as for the FS model. With this method, we find that the RP model fits the attenuation coefficients derived by *Meylan et al.* [2014] best, when $f=1.00$, $G\approx 9.2\times10^9$ Pa, and $\gamma\approx 6.9$ Pa s m^{-1}. Because the optimal factor is $f=1.00$, we also checked if the RP model makes better predictions when $f<1$, but that was not the case. The fit to the data is plotted in Figure 9 (solid blue line). We find a weighted sum of squared deviations of $\Delta\approx 2.2$, so the fit is not as good as with the FS model ($\Delta\approx 0.4$). Specifically, for these parameters, the RP model agrees well with the data for $T\gtrsim 11$ s, but underestimates the attenuation for lower periods. Other methods for finding G and γ can result in a better fit, however. For instance, by manually changing the parameters to $G\approx 3.2\times10^7$ Pa and $\gamma\approx 6.0$ Pa s m^{-1}, we obtain a fit with a weighted sum of squared deviations of $\Delta\approx 0.5$ (see dot-dashed blue line in Figure 9). However, with the new parameters the predicted wavelength is very close to the open water wavelength for all T, which seems unrealistic as an ice layer should change the wavelength.

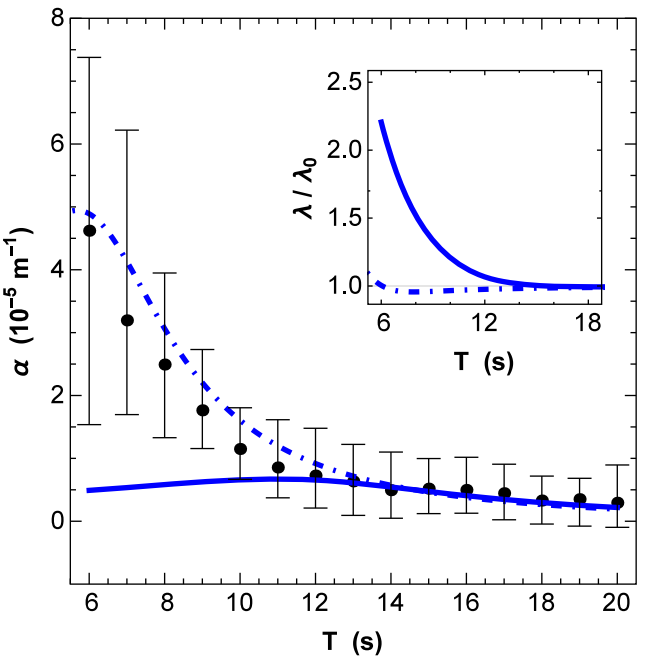

Figure 9. Same as Figure 8 for the RP model. The systematic optimization procedure described in the text (solid blue line) yields the optimized parameters $\lambda=1.0\,\lambda_0$, $G=9.2\times10^9$ Pa, $\gamma=6.9$ Pa s m^{-1}, $h=1$ m, and $H=4300$ m. The fit was improved by manually changing the parameters to $G\approx 3.2\times10^7$ Pa and $\gamma\approx 6.0$ Pa s m^{-1} (dot-dashed blue line).

7.3. WS Model

In contrast to the FS and RP models, the dispersion relation of the WS model cannot be inverted analytically, so we used Newton's method to estimate G_V numerically. The procedure is further complicated by the existence of multiple G_V solutions to the inverse problem. Consequently, for each data point considered, several pairs of positive rheological parameters (G,η) can be used to fit one of the many solutions of the WS dispersion relation to that data point. The number of possible calibrations can be reduced by demanding that $G\lesssim10^9$ Pa and $\eta\lesssim 1$ m^2 s^{-1} as suggested by *Wang and Shen* [2010], although we argued in section 7.1 that such restrictions are not physically justified for the types of empirical model considered here. Moreover, several or no solutions may satisfy these restriction criteria for a given set of parameters.

Table 1. A Sample of (G, η) Pairs That Solve the WS Inverse Problem at $T=10$ s and Satisfy the Restriction Criteria of *Wang and Shen* [2010][a]

G (Pa)	η ($m^2\ s^{-1}$)
6.4×10^5	1.1
3.7×10^1	4.8×10^{-9}
1.6×10^5	2.8×10^{-1}
9.2	2.2×10^{-10}

[a]The solutions were obtained for attenuation rates derived by *Meylan et al.* [2014]. The wavelength $\lambda=1.70\,\lambda_0$ was chosen such that the FS model fits best to the data. Other parameters are $h=1$ m and $H=4300$ m.

The fact that the WS model provides multiple solutions to the inverse problem makes its calibration difficult. Specifically, the optimization procedure devised in section 7.1 for the FS model cannot be used here as, even using Wang and Shen's restriction criteria for G and η, multiple solutions may exist for each wave period and wavelength. *Zhao and Shen* [2015] encountered the same issue, but we believe that they did not fully appreciate its severity. To simplify the calibration, we consider the measured attenuation rate at $T=10$ s only, i.e., $1.2\times10^{-5}\ m^{-1}$. Assuming $\lambda=1.70\,\lambda_0$, $h=1$ m, and $H=4300$ m, as for the FS model, we compute four possible calibrations that satisfy Wang and Shen's criteria. The four (G, η) pairs are listed in Table 1. Each of these pairs can then be used in the WS dispersion relation to predict the same mode $k=2\,\pi/\lambda+\mathrm{i}\,\alpha$. It is unclear, however, if this mode is the dominant mode k_{dom}^{WS} or any of the standard set of solutions, i.e., k_1^{WS}, k_2^{WS}, k_3^{WS}, k_4^{WS}, k_A^{WS}, or k_B^{WS}, defined in section 5. Therefore, we compute the standard solutions for each (G, η) pair in Table 1 and compare them with the value of k estimated from the data. We find that none of these (G, η) pairs predicts k as a dominant mode at $T=10$ s (i.e., one of the standard solutions $\neq k$ is dominant instead). That is, no matter which calibration we choose, the solution that fits the data is not the dominant one according to the dominance criteria (i) and (ii) discussed in section 5. This challenges the suitability of these criteria for selecting the mode with most geophysical relevance. Furthermore, k matches with one of the standard solutions for only one of the four pairs, i.e., $(G, \eta)=(1.6\times10^5\ \mathrm{Pa}, 2.8\times10^{-1}\ m^2\ s^{-1})$, in which case $k=k_1^{WS}$ while $k_{dom}^{WS}=k_2^{WS}$. We select this calibration for investigating the fit to the data.

The attenuation curves of k_1^{WS}, k_2^{WS}, and k_A^{WS} are shown in Figure 10 with the attenuation coefficients derived by *Meylan et al.* [2014], as these three solutions become alternatively dominant as the wave period changes. For $T\lesssim16$ s, k_2^{WS} dominates. Between $T\approx16$ s and 18 s, no solution satisfies both criteria (i) and (ii), but k_A^{WS} is closest to the open water wavelength, and is therefore considered dominant, following criterion (i) only. For $T\gtrsim18$ s, $k_{dom}^{WS}=k_1^{WS}$. As mentioned earlier, although $k_{dom}^{WS}=k_2^{WS}$ at $T=10$ s, the solution that fits the data point at $T=10$ s exactly (and for which the model was calibrated) is k_1^{WS}. In fact, $k_{dom}^{WS}=k_2^{WS}$ underestimates the attenuation in that regime, but k_1^{WS} and k_A^{WS} both fit well. Moreover, for $T\gtrsim18$ s, both k_A^{WS} and k_2^{WS} fit the data well, but k_1^{WS}, which is dominant, underestimates the attenuation rate (although within error bars). Interestingly, k_A^{WS} fits the observations within error bars for all T. The same is true for k_1^{WS}, although the agreement is not as good as with k_A^{WS}. When the criteria (i) and (ii) are applied (or just (i) if both cannot be satisfied simultaneously), we compute $\Delta\approx5.1$, while when at each T the best fitting solution is selected, we obtain $\Delta\approx0.2$. We also find $\Delta\approx0.2$ if we select k_A^{WS} for all

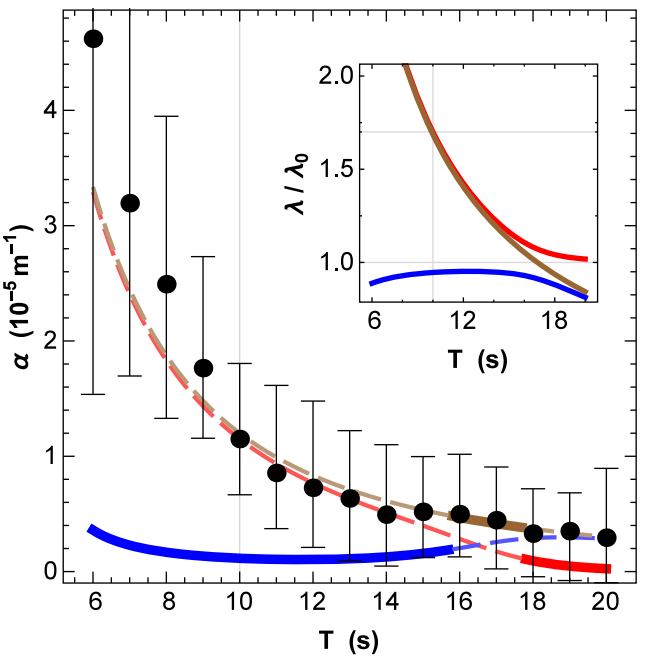

Figure 10. Same as Figure 8 for the WS model. The red, blue, and brown lines correspond to k_1^{WS}, k_2^{WS}, and k_A^{WS}, respectively. Lines in the main figure are solid if the solution is a dominant mode and dashed otherwise. The optimized parameters were $\lambda=1.70\,\lambda_0$, $G=1.6\times10^5$ Pa, $\eta=2.8\times10^{-1}\ m^2\ s^{-1}$, $h=1$ m, and $H=4300$ m, such that one solution (k_1^{WS} here) fits the data point at $T=10$ s exactly.

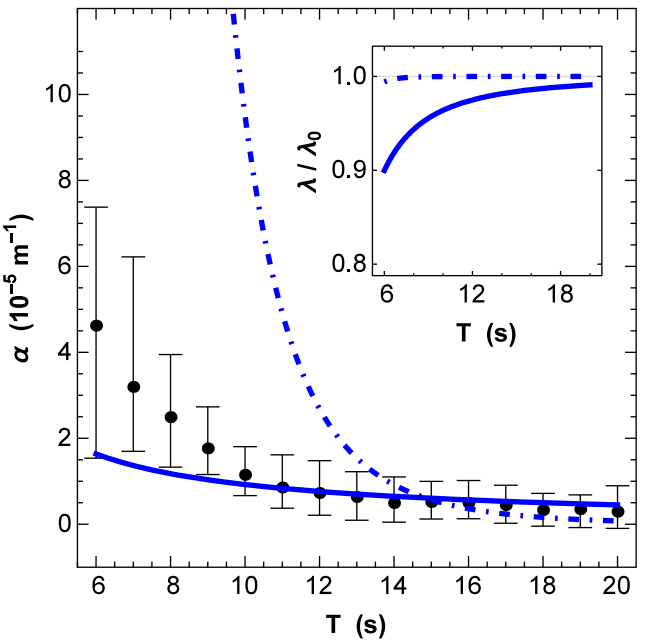

Figure 11. Same as Figure 8 for the thin viscous layer model of *Keller* [1998]. The blue solid and dot-dashed lines correspond to the calibrations $\eta = 15.7 \times 10^3$ m^2 s^{-1} and $\eta = 6.6$ m^2 s^{-1}, respectively.

periods. This shows that the WS model can potentially fit the data, but the dominant solution criteria (i) and (ii) need to be revised. It is not clear how the physical solution could be selected when observational data are not given, however.

The procedure was repeated by fitting the WS model to the data at $T = 16$ s, which confirmed the outcomes of our analysis.

7.4. WS Model Without Elasticity

In the previous sections, we found that all three viscoelastic models (WS, FS, and RP) can fit the attenuation coefficients derived by *Meylan et al.* [2014] for some values of the rheological parameters. Purely viscous rheological models have also been used to model wave propagation in ice-infested seas as mentioned in section 1, and have been calibrated with success for pancake ice [see e.g., *Doble et al.*, 2015]. It is then reasonable to investigate the fit to the attenuation data of *Meylan et al.* [2014] by a simpler viscous layer model, which does not include elastic effects. We consider the thin viscous layer model proposed by *Keller* [1998], which can be derived from the WS model by removing the elastic constant ($G = 0$ Pa), assuming small ice layer thickness ($h \ll g\,\omega^{-2}$), and small Reynolds number ($\omega\, h^2\, \eta^{-1} \ll 1$). This leads to the dispersion relation

$$\eta = \mathrm{i}\left(\tilde{\rho}\,\omega^2\,(\omega^2 - g\,h\,k^2) + k\,(g^2\,h\,k^2\,(\tilde{\rho}-\rho) - g\,\tilde{\rho}\,\omega^2 + h\,\rho\,\omega^4)\tanh(H\,k)\right) \Big/ \left(4\,k^2\,(\tilde{\rho}\,\omega^3 + k\,\omega\,(h\,\rho\,\omega^2 - g\,\tilde{\rho})\tanh(H\,k))\right), \tag{30}$$

which we have already solved for η.

At each period T, we numerically solve the imaginary part of (30), which does not involve η, for the wavelength λ. All other parameters are as before. We find two physically relevant solutions for λ at each T, both of which are very close to the respective open water wavelength. We substitute these into (30) to obtain η at any particular T. By taking the mean of all η for each group, we find two possible calibrations: $\eta = 15.7 \times 10^3$ m^2 s^{-1} and $\eta = 6.6$ m^2 s^{-1}, with $\Delta \approx 1.1$ and $\Delta > 3000$, respectively. The dominant solutions are easy to identify (as in the FS and RP models), and are visualized in Figure 11. A reasonable agreement is seen at high wave periods, but significant discrepancy is observed at low wave periods. We were not able to improve the fit of this model by manually changing η. This analysis suggests that elastic effects cannot be neglected in rheological models for MIZ-type ice covers.

8. Conclusions

In this work, we have considered three viscoelastic-type models for the attenuation of ocean waves propagating in the MIZ. All three models are empirical parameterizations of the observed attenuation phenomenon and describe the ice layer as a homogeneous viscoelastic continuum, which is fully characterized by a dispersion relation. We sought to determine the conditions under which the viscoelastic fluid model proposed by *Wang and Shen* [2010] (WS model) can be replaced by a simpler thin viscoelastic beam model. Two beam models were considered. In the first one (FS model), viscous effects are introduced into the constitutive relation of the thin

elastic beam, while in the second one (RP model), viscous effects appear as a friction term proportional to the vertical velocity in the equation of motion of the thin beam. The deviatoric stress-strain relation used in the FS model is identical to that of the WS model, so we were able to compare the solutions of their dispersion relations directly. We have then used wave data collected in the Antarctic MIZ and analyzed by *Meylan et al*. [2014] to calibrate the three models and assess their ability to predict wave attenuation in ice-covered seas.

Some major drawbacks associated with the WS model have been identified. First, the dispersion relation is difficult to solve numerically with some features requiring special numerical treatment, e.g., local maxima located close to roots in the contour plot of the dispersion relation. Second, the dispersion relation has many solutions of potential relevance, so identifying the one that has most geophysical relevance, referred to as the dominant solution, is not straightforward. Although *Wang and Shen* [2010] provide criteria to identify this mode, we found much evidence suggesting that these criteria are inappropriate in some circumstances. In particular, the solutions that best agree with observations do not satisfy the dominant mode criteria of *Wang and Shen* [2010]. Finally, there exist many solutions to the inverse problem of calibrating the rheological parameters of the WS model using measurements of waves traveling through ice. The inverse solutions are estimated numerically. No selection criteria have been advanced that provide good agreement with attenuation data and predict a dominant wave mode.

Unlike the WS model, the FS and the RP beam models have dispersion relations that can be solved in most situations using standard root finding techniques. Only two relevant solutions exist and the dominant mode is readily identified. It was demonstrated that the solutions of the FS dispersion relation are in close agreement with those of the WS model for a wide range of parameters. Discrepancies exist when the rheological elastic modulus and the viscosity are small, as shear forces in the WS fluid model become dominant. This does not tend to favor one model over the other, however, as the parameters of these models are entirely empirical, with no physical relevance.

A calibration procedure was conceived to fit the two beam models to the attenuation coefficients derived by *Meylan et al*. [2014]. The dispersion relations of both the FS and RP models can be inverted analytically for the rheological parameters and the solution is unique. We overcame the lack of wavelength data in our procedure using an optimization technique which estimates the wavelength at each data point that provides the best fit. The FS and RP models were found to be able to predict wave attenuation rates that fit all data points within error bars. Although either of these models can be used to predict wave attenuation of this data set, it would be unwise to generalize this finding to other situations.

The WS model was also found to predict attenuation rates that fit the data, but they correspond to wave modes that are not dominant when the criteria of *Wang and Shen* [2010] are used. It is thus clear that the dominance criteria cannot be used unambiguously to predict wave attenuation with the WS model. When the best fitting wave mode, regardless of type, is selected at each period, however, the WS model is closer to the data than the FS and RP models.

The simpler thin viscous layer model of *Keller* [1998] was also considered. We found that the viscous layer model predicts a worse fit to the attenuation data than the WS, FS, and RP models, suggesting that elasticity may be an important component of fitting these models to MIZ data.

Finally, we conclude this study with the following recommendations for modeling wave attenuation in ice-covered seas:

1. In this article, we found that the dominance criteria of the WS model need to be revised, if they are to be used in spectral wave models such as WAVEWATCH III® to predict attenuation; alternatively, simpler continuum models such as the FS or RP models could be used.
2. We reiterate the fact that substantial additional wave attenuation data obtained for a range of ice conditions are needed to calibrate and test the validity of rheological models such as the WS, FS, and RP models, including simultaneous measurements of wave periods, attenuation coefficients, and wavelengths, which is not logistically achievable with contemporary (in situ or remote sensing) measurement techniques.
3. From a modeling perspective, process-based models (e.g., scattering, floe collisions, wave breaking, etc.) offer a viable and more physically defensible alternative to rheological models, as they are capable of estimating wave attenuation directly in terms of observable ice conditions, such as floe size distribution and ice concentration.

Acknowledgments
J.E.M.M. was supported by the University of Otago Postgraduate Scholarship. F.M. and V.A.S. were supported by the Office of Naval Research Departmental Research Initiative "Sea State and Boundary Layer Physics of the Emerging Arctic Ocean" (award N00014-131-0279), the EU FP7 grant (SPA-2013.1.1-06), and the University of Otago. The authors have enjoyed discussions with H. Shen and E. Rogers, which have improved the work reported in this paper. We are grateful to L. Bennetts (luke.bennetts@adelaide.edu.au) for providing wave attenuation data from *Meylan et al*. [2014]. The source code necessary to reproduce the figures presented in this article is available from the authors upon request (jmosig@maths.otago.ac.nz).

References

Bennetts, L. G., and V. A. Squire (2012), On the calculation of an attenuation coefficient for transects of ice-covered ocean, *Proc. R. Soc. A*, *468*(2137), 136–162, doi:10.1098/rspa.2011.0155.

Collins, C. O., W. E. Rogers, A. Marchenko, and A. V. Babanin (2015), In situ measurements of an energetic wave event in the Arctic marginal ice zone, *Geophys. Res. Lett.*, *42*, 1863–1870, doi:10.1002/2015GL063063.

De Carolis, G., and D. Desiderio (2002), Dispersion and attenuation of gravity waves in ice: A two-layer viscous fluid model with experimental data validation, *Phys. Lett. A*, *305*(6), 399–412, doi:10.1016/S0375-9601(02)01503-7.

Doble, M. J., and J.-R. Bidlot (2013), Wave buoy measurements at the Antarctic sea ice edge compared with an enhanced ECMWF WAM: Progress towards global waves-in-ice modelling, *Ocean Modell.*, *70*, 166–173, doi:10.1016/j.ocemod.2013.05.012.

Doble, M. J., G. De Carolis, M. H. Meylan, J.-R. Bidlot, and P. Wadhams (2015), Relating wave attenuation to pancake ice thickness, using field measurements and model results: Waves in Pancakes, *Geophys. Res. Lett.*, *42*, 4473–4481, doi:10.1002/2015GL063628.

Evans, D. V., and T. V. Davies (1968), *Wave-Ice Interaction*, Castle Point Stn., Davidson Lab., Stevens Inst. of Technol., Hoboken, N. J.

Flügge, W. (1975), *Viscoelasticity*, Springer, Berlin.

Fox, C., and V. A. Squire (1994), On the oblique reflexion and transmission of ocean waves at shore fast sea ice, *Philos. Trans. R. Soc. London A*, *347*(1682), 185–218, doi:10.1098/rsta.1994.0044.

GEBCO (2014), GEBCO Gridded Bathymetry Data. [Available at http://www.gebco.net/data_and_products/gridded_bathymetry_data/.]

Greenhill, A.-G. (1886), Wave motion in hydrodynamics, *Am. J. Math.*, *9*, 62–96.

Jeffries, M. O., J. E. Overland, and D. K. Perovich (2013), The Arctic shifts to a new normal, *Phys. Today*, *66*(10), 35–40, doi:10.1063/PT.3.2147.

Keller, J. B. (1998), Gravity waves on ice-covered water, *J. Geophys. Res.*, *103*(C4), 7663–7669, doi:10.1029/97JC02966.

Kohout, A., and M. Williams (2013), Waves in-ice observations made during the SIPEX II voyage of the Aurora Australis, 2012, Aust. Antarct. Data Cent., doi:10.4225/15/53266BEC9607F.

Kohout, A. L., and M. H. Meylan (2008), An elastic plate model for wave attenuation and ice floe breaking in the marginal ice zone, *J. Geophys. Res.*, *113*, C09016, doi:10.1029/2007JC004434.

Kohout, A. L., M. H. Meylan, and D. R. Plew (2011), Wave attenuation in a marginal ice zone due to the bottom roughness of ice floes, *Ann. Glaciol.*, *52*(57), 118–122.

Kohout, A. L., M. J. M. Williams, S. M. Dean, and M. H. Meylan (2014), Storm-induced sea-ice breakup and the implications for ice extent, *Nature*, *509*(7502), 604–607, doi:10.1038/nature13262.

Kohout, A. L., B. Penrose, S. Penrose, and M. J. Williams (2015), A device for measuring wave-induced motion of ice floes in the Antarctic marginal ice zone, *Ann. Glaciol.*, *56*(69), 415–424, doi:10.3189/2015AoG69A600.

Kwok, R., and D. A. Rothrock (2009), Decline in Arctic sea ice thickness from submarine and ICES at records: 1958–2008, *Geophys. Res. Lett.*, *36*, L15501, doi:10.1029/2009GL039035.

Liu, A. K., and E. Mollo-Christensen (1988), Wave propagation in a solid ice pack, *J. Phys. Oceanogr.*, *18*(11), 1702–1712, doi:10.1175/1520-0485(1988)018<1702:WPIASI>2.0.CO;2.

Liu, A. K., P. W. Vachon, C. Y. Peng, and A. Bhogal (1992), Wave attenuation in the marginal ice zone during LIMEX, *Atmos. Ocean*, *30*(2), 192–206, doi:10.1080/07055900.1992.9649437.

Meier, W. N., D. Gallaher, and G. G. Campbell (2013), New estimates of Arctic and Antarctic sea ice extent during September 1964 from recovered Nimbus I satellite imagery, *Cryosphere*, *7*(2), 699–705, doi:10.5194/tc-7-699-2013.

Meylan, M. H., L. G. Bennetts, and A. L. Kohout (2014), In situ measurements and analysis of ocean waves in the Antarctic marginal ice zone, *Geophys. Res. Lett.*, *41*, 5046–5051, doi:10.1002/2014GL060809.

Newyear, K., and S. Martin (1999), Comparison of laboratory data with a viscous two-layer model of wave propagation in grease ice, *J. Geophys. Res.*, *104*(C4), 7837–7840, doi:10.1029/1999JC900002.

Robinson, N. J., and S. C. Palmer (1990), A modal analysis of a rectangular plate floating on an incompressible liquid, *J. Sound Vibration*, *142*(3), 453–460, doi:10.1016/0022-460X(90)90661-I.

Rogers, W. E., and M. D. Orzech (2013), Implementation and testing of ice and mud source functions in WAVEWATCH III (registered trademark), technical report no. NRL/MR/7320–13-9462, Office of Naval Research, One Liberty Center, Arlington, Va.

Simpkins, G. R., L. M. Ciasto, and M. H. England (2013), Observed variations in multidecadal Antarctic sea ice trends during 1979–2012, *Geophys. Res. Lett.*, *40*, 3643–3648, doi:10.1002/grl.50715.

Squire, V. A. (2007), Of ocean waves and sea-ice revisited, *Cold Reg. Sci. Technol.*, *49*(2), 110–133, doi:10.1016/j.coldregions.2007.04.007.

Squire, V. A. (2011), Past, present and impendent hydroelastic challenges in the polar and subpolar seas, *Philos. Trans. R. Soc. London A*, *369*(1947), 2813–2831, doi:10.1098/rsta.2011.0093.

Squire, V. A., and A. Allan (1980), Propagation of flexural gravity waves in sea ice, in *Sea Ice Processes and Models*, edited by R. Pritchard, pp. 327–338, Univ. of Wash. Press, Seattle, Wash.

Squire, V. A., and C. Fox (1992), On ice coupled waves: A comparison of data and theory, in *Advances in Ice Technology, Proceedings of 3rd International Conference on Ice Technology*, edited by T. K. Murthy, W. M. Sackinger, and P. Wadhams, pp. 269–280, Computational Mechanics Publications, Southampton, U. K.

Squire, V. A., J. P. Dugan, P. Wadhams, P. J. Rottier, and A. K. Liu (1995), Of ocean waves and sea ice, *Annu. Rev. Fluid Mech.*, *27*(1), 115–168, doi:10.1146/annurev.fl.27.010195.000555.

Stroeve, J., M. M. Holland, W. Meier, T. Scambos, and M. Serreze (2007), Arctic sea ice decline: Faster than forecast, *Geophys. Res. Lett.*, *34*, L09501, doi:10.1029/2007GL029703.

Thomson, J., and W. E. Rogers (2014), Swell and sea in the emerging Arctic Ocean, *Geophys. Res. Lett.*, *41*, 3136–3140, doi:10.1002/2014GL059983.

Tietsche, S., J. J. Day, V. Guemas, W. J. Hurlin, S. P. E. Keeley, D. Matei, R. Msadek, M. Collins, and E. Hawkins (2014), Seasonal to interannual Arctic sea ice predictability in current global climate models, *Geophys. Res. Lett.*, *41*, 1035–1043, doi:10.1002/2013GL058755.

Tolman, H. L., and The WAVEWATCH III® Development Group (2014), User manual and system documentation of WAVEWATCH III® version 4.18, *Tech. Note 316*, 282 pp., NOAA/NWS/NCEP/MMAB, U. S. Department of Commerce, Nat. Ocean. Atmos. Admin., College Park, Md.

Wadhams, P. (1973), The effect of a sea ice cover an ocean surface waves, PhD thesis, Univ. of Cambridge, Cambridge, U. K.

Wadhams, P. (1986), The seasonal ice zone, in *The Geophysics of Sea Ice, NATO ASI Ser.*, edited by N. Untersteiner, pp. 825–991, Springer, N. Y.

Wadhams, P., and B. Holt (1991), Waves in frazil and pancake ice and their detection in Seasat synthetic aperture radar imagery, *J. Geophys. Res.*, *96*(C5), 8835–8852, doi:10.1029/91JC00457.

Wadhams, P., V. A. Squire, D. J. Goodman, A. M. Cowan, and S. C. Moore (1988), The attenuation rates of ocean waves in the marginal ice zone, *J. Geophys. Res.*, *93*(C6), 6799–6818, doi:10.1029/JC093iC06p06799.

Wadhams, P., F. F. Parmiggiani, G. de Carolis, D. Desiderio, and M. J. Doble (2004), SAR imaging of wave dispersion in Antarctic pancake ice and its use in measuring ice thickness, *Geophys. Res. Lett.*, *31*, L15305, doi:10.1029/2004GL020340.

Wang, R., and H. H. Shen (2010), Gravity waves propagating into an ice-covered ocean: A viscoelastic model, *J. Geophys. Res.*, *115*, C06024, doi:10.1029/2009JC005591.

Williams, T. D., L. G. Bennetts, V. A. Squire, D. Dumont, and L. Bertino (2013a), Wave-ice interactions in the marginal ice zone. Part 2: Numerical implementation and sensitivity studies along 1d transects of the ocean surface, *Ocean Modell.*, *71*, 92–101, doi:10.1016/j.ocemod.2013.05.011.

Williams, T. D., L. G. Bennetts, V. A. Squire, D. Dumont, and L. Bertino (2013b), Wave-ice interactions in the marginal ice zone. Part 1: Theoretical foundations, *Ocean Modell.*, *71*, 81–91, doi:10.1016/j.ocemod.2013.05.010.

Wolfram Research, Inc. (2014), Mathematica, Wolfram Research, Inc., Champaign, Ill.

Young, I. R., S. Zieger, and A. V. Babanin (2011), Global trends in wind speed and wave height, *Science*, *332*(6028), 451–455, doi:10.1126/science.1197219.

Zhao, X., and H. H. Shen (2015), Wave propagation in frazil/pancake, pancake, and fragmented ice covers, *Cold Reg. Sci. Technol.*, *113*, 71–80, doi:10.1016/j.coldregions.2015.02.007.